

# CHAM-net: A Contrastive Hierarchical Adaptive Meta-network for Robust Global Methane Flux Prediction

Rongchao Dong<sup>1</sup>, Yiming Sun<sup>1</sup>, Shuo Chen<sup>2</sup>, Youmi Oh<sup>3,4</sup>, Licheng Liu<sup>5</sup>, Yiqun Xie<sup>6</sup> and Xiaowei Jia<sup>1</sup>

<sup>1</sup>University of Pittsburgh, <sup>2</sup>Purdue University, <sup>3</sup>University of Colorado Boulder, <sup>4</sup>NOAA Global Monitoring Laboratory, <sup>5</sup>University of Wisconsin–Madison and <sup>6</sup>University of Maryland {rongchaodong, yis108, xiaowei}@pitt.edu, chen4371@purdue.edu, youmi.oh@noaa.gov, licheng.liu@wisc.edu, xie@umd.edu

## Abstract

Methane is a potent greenhouse gas that significantly contributes to global warming. However, accurately estimating global methane emissions and consumption remains challenging due to the complex interactions among environmental drivers that may vary across spatial and temporal scales. Prior data-driven methods often overlook the inherent spatiotemporal heterogeneity of ecosystems, failing to explicitly capture site-specific characteristics and cross-year evolutionary dynamics. To address these issues, we propose the **Contrastive Hierarchical Adaptive Meta-network (CHAM-net)**, a novel framework that explicitly learns from historical context to capture site-specific dynamics. CHAM-net employs a hierarchical encoder–decoder architecture, in which the encoder captures site-specific characteristics from historical data and then dynamically conditions the decoder to generate the final prediction. Experimental results demonstrate that CHAM-net consistently outperforms all baseline methods on both simulation and observational datasets for methane emission and consumption, achieving nRMSE values as low as 0.43 and 0.88 with corresponding R<sup>2</sup> scores up to 0.97 and 0.68 for emission prediction.

## 1 Introduction

Methane ( $CH_4$ ) is the second most significant greenhouse gas contributing to global warming after carbon dioxide ( $CO_2$ ) and is responsible for about 30% of the increase in global temperature since the industrial revolution [Stocker, 2014]. Unlike carbon dioxide, methane is chemically reactive in the atmosphere and therefore has a relatively short atmospheric lifetime of about 9 years [Saunois *et al.*, 2025]. This short lifetime means that reducing methane emissions can deliver rapid climate benefits, including slower warming rates, reduced climate extremes, and improved air quality [Mar *et al.*, 2022], making methane mitigation one of the most effective near-term strategies for protecting human health, ecosystems, and vulnerable communities [Ocko *et al.*, 2021].

Traditional approaches primarily rely on process-based biogeochemistry models [Zhuang *et al.*, 2004; Tian *et al.*,

2015; Zhang *et al.*, 2017] to simulate and estimate the natural methane cycle. By incorporating the theoretical understanding of methane ecosystem dynamics with the key environmental drivers (e.g., soil features and temperatures), these models can be extended to enable global methane prediction and subsequent budget estimation. However, they are often limited by rigid and extensive parameterization, leading to biased prediction and substantial computational requirements when applied over large regions and long time periods. Recently, data-driven machine learning (ML) methods [Kim *et al.*, 2020; Irvin *et al.*, 2021; Luo *et al.*, 2023; Saha *et al.*, 2025] have emerged as a promising alternative, demonstrating strong capability in capturing non-linear relationships between environmental drivers and methane flux. Existing works have further explored knowledge transfer (e.g., pretraining and fine-tuning) from simulated data to sparse real observations (e.g., collected from eddy covariance towers) to improve the prediction accuracy [Sun *et al.*, 2025].

However, existing ML methods typically assume diverse methane sites across space are governed by a shared set of global parameters, and neglect the spatiotemporal heterogeneity. In particular, methane emission and consumption patterns are highly site-specific because different sites can respond differently to similar input drivers due to the underlying variations in microbial communities and soil properties. For example, Figure 1 (a) compares annual emissions at three sites (US.Myb [Matthes *et al.*, 2018], DE.Hte [Koebsch and Jurasinski, 2018], and US.ORv [Bohrer and Morin, 2015]) in 2013. These sites exhibit clearly different emission patterns and magnitudes. Without fully leveraging site-specific context, existing models tend to predict averaged values, which could underestimate high-valued regions and overestimate low-valued regions (e.g., the significant differences between sites DE.Hte and US.ORv in Figure 1 (a)).

Additionally, current ML methods mostly utilize short-term data (e.g., data from the current year) and focus on capturing short-term temporal dynamics (e.g., seasonal changes of precipitation). However, they are not designed to capture the impact of many long-term processes (e.g., slow changes in plant cover, soil composition) that also affect methane dynamics over years. As shown in Figure 1 (b), for site FI.Lom [Lohila *et al.*, 2010], we can observe a sustained decline in total methane emissions from 2006 to 2009, reflecting a site-specific cross-year temporal evolution pattern.

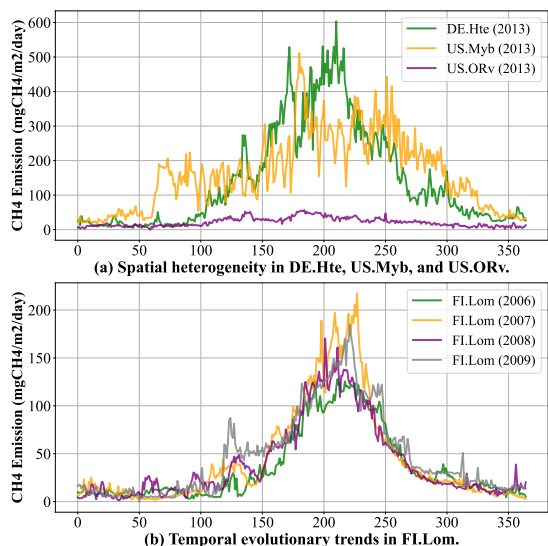


Figure 1: spatiotemporal heterogeneity within the datasets.

To address these limitations, we propose the **Contrastive Hierarchical Adaptive Meta-network (CHAM-net)**, a novel framework that explicitly learns site-specific dynamics from multi-year historical data. While many site-specific characteristics (e.g., microbial communities and soil properties) are not directly observable, their influence is often manifested in the long-term trend shown in each site’s historical methane record. CHAM-net therefore leverages each site’s historical methane data to capture these latent characteristics and improve current-year prediction. Specifically, CHAM-net adopts a hybrid meta-learning mechanism [Hospedales *et al.*, 2021] in which the inner model encodes multi-year environmental and methane dynamics into learnable representations to summarize site-specific characteristics (e.g., temporal patterns and scales), while the outer model leverages these learned representations to condition the current-year prediction process. This design shifts prediction from a global model to a site-aware estimation. Additionally, optimizing the outer loop helps shape the inner-loop learning task, which enables effective extraction of site-specific information.

**Connections to the social good.** By applying our advanced AI architecture to resolve the spatiotemporal heterogeneity of methane ecosystems, this work significantly reduces uncertainties in natural methane budgets and improves process-level understanding, thereby enabling more effective and accurate methane mitigation strategies in support of the Global Methane Pledge [Malley *et al.*, 2023]. These advances directly contribute to multiple UN Sustainable Development Goals (<https://sdgs.un.org/goals>), including Climate Action, Good Health and Well-Being, and Life on Land, by informing near-term climate mitigation pathways and air-quality prediction, and supporting sustainable wetland management.

This paper is conducted in active collaboration with domain experts from NOAA Global Monitoring Laboratory, University of Wisconsin-Madison, University of Maryland, and Purdue University, who are internationally recognized experts in global methane observations, process understanding, and atmospheric data assimilation. These scientists

contribute domain knowledge, observational constraints, and evaluate the real-world impact of these novel methodologies throughout model development, training, and interpretation.

### Technical Contributions.

- We identify inherent site heterogeneity as a key factor underlying the inaccurate predictions of the current models, and show that historical data encodes critical site-specific information essential for effective site prediction.
- We propose CHAM-net, an encoder–decoder hybrid meta-learning framework that dynamically leverages historical data to calibrate site-specific predictions for the current year.
- We evaluate CHAM-net on extensive methane emission and consumption datasets, including both simulation and observational data. Experimental results show that CHAM-net consistently outperforms all baselines in all datasets, achieving an nRMSE of 0.88 and an  $R^2$  of 0.68 in FLUXNET emission dataset.

## 2 Problem Formulation

The task of global methane flux prediction can be formulated as a site-level time-series regression problem. For each site  $i \in \{1, \dots, N\}$ , we are given a sequence of environmental drivers (e.g., soil properties and temperature) over a time period, denoted as  $X_i = \{x_1, x_2, \dots, x_T\}$ , where each  $x_t \in \mathbb{R}^D$  is a feature vector of dimension  $D$  at time  $t$  (e.g., a specific date),  $D$  is the total number of input drivers, and  $T$  is the length of each sequence. Following prior works in methane prediction and other environmental monitoring tasks [Liu *et al.*, 2024a; Sun *et al.*, 2025], we cut the data into yearly sequences (i.e.,  $T=365$ ) to facilitate modeling seasonal patterns. The goal is to predict the methane flux for the corresponding year  $Y_i = \{y_1, y_2, \dots, y_T\}$ , where  $y_t \in \mathbb{R}$  is the target label, e.g., methane emission or consumption. In our proposed method, we also leverage multi-year historical records. For each site  $i$ , we use  $X_i^{(k)}$  and  $Y_i^{(k)}$  to represent the environmental drivers and methane data from a historical year  $k \in \{1, \dots, K\}$ .

The datasets used in this paper can be categorized into simulation and observational datasets, each with distinct characteristics as follows:

- **Simulation Dataset** We use process-based simulation datasets, which incorporate biogeochemical processes to simulate methane fluxes by solving differential equations. Given globally available input drivers, they enable estimation of methane fluxes at the global scale. However, due to the complexity of model computations and uncertainties in multiple input drivers, the highest spatial resolution is limited to 0.5 degree, corresponding to approximately 3,000  $\text{km}^2$  per grid.
- **Observational Dataset** In observational datasets, both input drivers and methane fluxes are directly measured at each site using eddy covariance techniques, providing real-world ground truth observations. However, these sites are spatially sparse and geographically discontinuous, with footprints on the order of hundreds of square meters. Moreover, observational datasets cover substantially shorter time spans than simulation datasets. The details of the datasets used in this paper are provided in Section 4.1.

### 3 Design and Methodology

In this section, we introduce the main design of CHAM-net (Contrastive Hierarchical Adaptive Meta-network) architecture, which addresses the aforementioned problems and leverages historical information to improve predictions.

#### 3.1 Model Overview

The proposed CHAM-net model explicitly incorporates historical information to learn site-specific characteristics and long-term dynamics. By employing a hybrid hierarchical meta-learning architecture, the model extracts the most informative historical trends and scales for each site. These learned site-specific representations are then injected into the decoder and combined with current-year inputs to improve the final prediction.

Figure 2 illustrates the overall architecture of the CHAM-net model. For each site, a configurable length of historical years’ data is used as the **support set**, while the current year data forms the **query set**. When the historical year length exceeds one year, a cross-attention module is first applied to compute each year’s relevance to the current-year inputs. The attention weights are then used to extract context-aware representations capturing local characteristics that influence current-year dynamics. These representations are then propagated to the decoder stage to guide the final prediction.

The workflow consists of two hierarchical phases:

- **Context Encoder.** The context encoder is designed to extract representations for capturing site-specific characteristics that affect current-year dynamics. Although many of these characteristics are not directly observable, they can be inferred from the dynamic responses of methane fluxes  $Y$  to environmental drivers  $X$ , i.e.,  $Y = f(X; \theta)$ . The key idea of the context encoder is to *inversely* infer these characteristics from historical methane data, by embedding them in a site-specific representation that serves as the parameters  $\theta$  for the function  $f$ . However, directly inferring the  $\theta$  as the full parameterization of the function  $f$  may not precisely capture the site-specific characteristics as the mapping is also influenced by many confounding factors. Hence, we reformulate the model  $f$  as  $Y = f(g(X); \theta)$ , where  $g$  serves as a global feature extractor (via a bidirectional GRU) that captures shared underlying processes while  $\theta$  parameterizes the site-specific information. The extractor  $g$  is learned end-to-end under supervised training, which helps better define and stabilize the inverse problem for the target task. A contrastive learning objective is further introduced to amplify inter-site differences, which ensures the discrimination of site-specific characteristics.

- **Adaptive Decoder.** The resulting site-specific representations are then transformed and injected into the hidden state of a Long Short-Term Memory (LSTM) [Hochreiter and Schmidhuber, 1997]-based decoder. The decoder shares parameters across all sites, but conditions its temporal dynamics on the injected site context. The final output of methane fluxes is produced from this context-enhanced hidden state.

The model is trained through a bi-level optimization process. The inner-loop optimization aims to extract site-specific representations from historical data observations. In the outer

loop, the model utilizes these representations to condition and enhance the prediction, while updating model parameters to optimize predictive performance and to shape the inner-loop objective.

In the following, we provide details of the model components as well as the training process.

#### 3.2 Context Encoder

The goal of the encoder is to convert the historical support set  $\mathcal{S}^{(k)} = \{(X_i^{t,(k)}, Y_i^{t,(k)})\}_{t=1}^T$  into a compact context-aware representation  $\mathbf{W}_i$  for each site  $i$ , and then use it to enhance the decoder through site-specific conditioning.

**BiGRU Module.** We first encode data from each historical year  $k$  using a bidirectional GRU:

$$\mathbf{G}_i^{(k)} = \text{BiGRU}(\mathbf{X}_i^{(k)}) \in \mathbb{R}^{T \times 2H}, \quad (1)$$

where  $H$  is the size of the hidden dimension.

**Site-specific MLP.** To capture the site-specific characteristics, we assign each site  $i$  a dedicated MLP projection head parameterized by  $\mathbf{W}_i^k$ , which can be represented by:

$$\hat{\mathbf{Y}}_i^{(k)} = \mathbf{G}_i^{(k)} \mathbf{W}_i^k + b_i, \quad (2)$$

where  $\mathbf{W}_i^k \in \mathbb{R}^{2H \times 1}$  and  $b_i \in \mathbb{R}$ .  $\hat{\mathbf{Y}}_i^{(k)}$  represents the predicted labels of year  $k$ , which are later used to compute the inner-loop loss.

In our proposed method, we use the learned  $\mathbf{W}_i^k$  as the representation of site-specific behavior. The MLP weights effectively distill rich historical information from both the drivers and methane fluxes into a compact representation. The dimensionality of  $\mathbf{W}_i^k$  can be adjusted based on the output dimension of the previous GRU layer.

**Year-wise Attention.** When incorporating multiple historical years (i.e.,  $K > 1$ ), we weight each year based on its relevance to the current-year prediction. We therefore compute attention weights that measure the year-wise importance  $\alpha_i^{(k)}$  of each historical year, as follows:

$$\alpha_i^{(k)} = \text{Attn}(\mathbf{X}_i^{(0)}, \mathbf{X}_i^{(k)}), \quad \text{s.t.}, \quad \sum_{k=1}^K \alpha_i^{(k)} = 1, \quad (3)$$

where  $\mathbf{X}_i^{(0)}$  is the current-year inputs. We employ the standard multiple-head attention mechanism to calculate the similarity between the current year and the historical years, and then normalize the attention weights across  $K$  historical years via softmax. The attention weights are used in the outer-loop for aggregating  $\mathbf{W}_i^k$  from historical years, which will be discussed in Section 3.3.

**Contrastive Learning.** To better ensure site discrimination and encode persistent site characteristics (e.g., long-term scaling and trend patterns) into  $\mathbf{W}_i^k$ , we introduce a contrastive objective directly defined over the site-specific representation  $\mathbf{W}_i^k$ . We treat the representation from the same site but different years as positive pairs ( $\mathbf{W}_i^k, \mathbf{W}_i^+$ ) and other sites in the batch as negatives. The contrastive loss is Info Noise-Contrastive Estimation (InfoNCE) loss, which is defined as:

$$\mathcal{L}_{cont} = -\log \frac{\exp(\text{sim}(\mathbf{W}_i^k, \mathbf{W}_i^+)/\tau)}{\sum_{j=1}^B \exp(\text{sim}(\mathbf{W}_i^k, \mathbf{W}_j)/\tau)}, \quad (4)$$

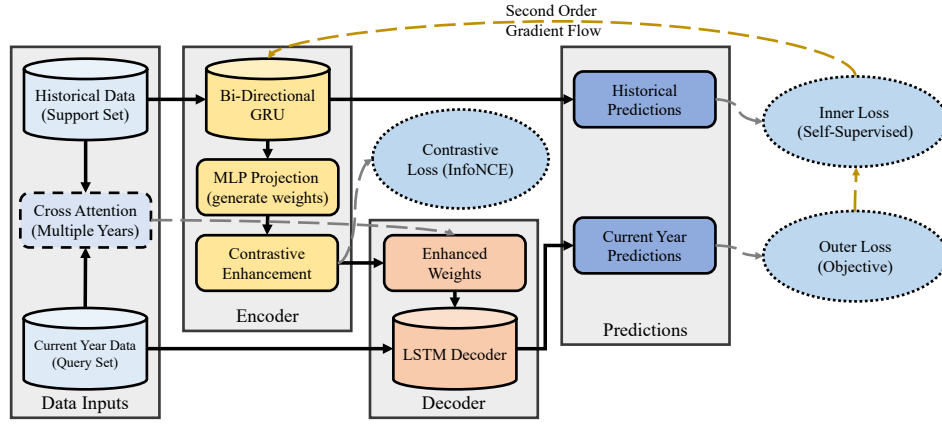


Figure 2: CHAM-net structure overview.

287 where  $B$  is the batch size,  $\text{sim}(\cdot)$  is the cosine similarity, and  
 288  $\tau$  is the configurable temperature parameter.  
 289 To improve the robustness of site-specific representations,  
 290 we adopt a stochastic perturbation method to augment the  
 291 generated  $\mathbf{W}_i^k$  in contrastive learning:

$$\tilde{\mathbf{W}}_i^k = \mathbf{W}_i^k + \epsilon, \quad \epsilon \sim \mathcal{N}(\mathbf{0}, \sigma^2 \mathbf{I}), \quad (5)$$

292 This augmentation encourages the embeddings to remain  
 293 stable under small variations of site-specific parameters.

### 294 3.3 Adaptive Decoder

295 The decoder serves as the base-learner that leverages the  
 296 outcome of the encoder to condition the actual flux pre-  
 297 diction on the Query Set  $\mathcal{Q}_i = \{X_{curr}^t\}_{t=1}^T$ . In our im-  
 298 plementation, the decoder is an LSTM-based model. We  
 299 adopt LSTM because LSTM-based architectures have con-  
 300 sistent performance in prior methane flux prediction studies [Luo *et al.*, 2023; Chen *et al.*, 2024; Sun *et al.*, 2025].

303 We first aggregate  $\tilde{\mathbf{W}}_i^k$  from multiple historical years using  
 304 attention weights  $\alpha_i^{(k)}$ , and then project the site-specific em-  
 305 bedding into the hidden state space of the decoder:

$$\tilde{\mathbf{z}}_i = \phi\left(\sum_{k=1}^K \alpha_i^{(k)} \tilde{\mathbf{W}}_i^k\right), \quad (6)$$

306 where  $\phi(\cdot)$  is a fully connected projection.  
 307 The  $\tilde{\mathbf{z}}_i$  will be further normalized with the original hidden  
 308 state of the LSTM decoder with a learnable weight  $\beta_i$ :

$$\tilde{\mathbf{h}}_i = \frac{\tilde{\mathbf{h}}_i + \beta_i \tilde{\mathbf{z}}_i}{1 + |\beta_i|}, \quad (7)$$

309 Then the final prediction is obtained by putting the current-  
 310 year inputs and the enhanced hidden state into the LSTM  
 311 decoder:

$$\hat{\mathbf{Y}}_i^{(0)} = \text{LSTM}_\psi(\mathbf{X}_i^{(0)}, \tilde{\mathbf{h}}_i), \quad (8)$$

312 where  $\psi$  denotes the other parameters of the LSTM, and  
 313  $\hat{\mathbf{Y}}_i^{(0)}$  is the predicted current-year labels.

### 314 3.4 Optimization and Loss Functions

315 The training of CHAM-net is formulated as a bilevel op-  
 316 timization problem, involving nested inner- and outer-loop

loss computations and the corresponding bilevel backpropaga- 317  
 tion process. The second-order backpropagation gradient 318  
 flow is illustrated in Figure 2. 319

**Inner-loop Reconstruction Loss.** The inner-loop objective 320  
 is designed to extract site representations using historical in- 321  
 formation. It consists of a historical reconstruction loss and 322  
 a contrastive enhancement loss: 323

$$\mathcal{L}_{\text{inner}}(\theta) = \mathcal{L}_{\text{hist}}(\theta) + \lambda_{\text{con}} \mathcal{L}_{\text{con}}(\theta), \quad (9)$$

where  $\theta = \{\mathbf{W}_i^k\}_{k=1}^K$  is the parameters in the inner-loop, 324  
 $\mathcal{L}_{\text{con}}(\theta)$  is the contrastive loss defined in Equation 4, and 325  
 $\lambda_{\text{con}}$  is a configurable hyperparameter that controls the con- 326  
 tribution of the contrastive loss. The historical reconstruc- 327  
 tion loss  $\mathcal{L}_{\text{hist}}(\theta)$  is defined as: 328

$$\mathcal{L}_{\text{hist}}(\theta) = \frac{1}{N} \sum_{i=1}^N \sum_{k=1}^K \alpha_i^{(k)} \left\| \hat{\mathbf{Y}}_i^{(k)} - \mathbf{Y}_i^{(k)} \right\|_2^2, \quad (10)$$

where  $N$  is the total number of sites in training. 329  
 The encoder parameters are updated through a differentiable 330  
 inner optimization step: 331

$$\theta' = \theta - \gamma \nabla_{\theta} \mathcal{L}_{\text{inner}}(\theta), \quad (11)$$

where  $\gamma$  is the inner learning rate. 332  
**Outer-loop Objective.** The outer-loop takes the learned rep- 333  
 resentation and performs current-year prediction, and the 334  
 loss is calculated by the mean squared error across all the 335  
 training sites: 336

$$\mathcal{L}_{\text{outer}}(\psi, \theta^*) = \frac{1}{N} \sum_{i=1}^N \left\| \hat{\mathbf{Y}}_i^{(0)}(\theta', \psi) - \mathbf{Y}_i^{(0)} \right\|_2^2 \quad (12)$$

The outer optimization updates the parameters  $\psi$  for both 337  
 the encoder and decoder parameters, i.e., the BiGRU pa- 338  
 rameters in the encoder and the LSTM parameters in the 339  
 decoder.  $\theta^*$  represents the updated site-specific representations 340  
 obtained from the inner-loop (via Eq. 11). Given that  $\theta^*$  341  
 also contributes to the final prediction, the outer-loop errors 342  
 are backpropagated to the representations  $\theta$ , which forms a 343  
 second-order gradient flow during the training process. 344  
 The complete training objective is formulated as follows: 345

$$\begin{aligned} \min_{\psi} \quad & \mathcal{L}_{\text{outer}}(\psi, \theta^*) \\ \text{s.t.} \quad & \theta^* = \arg \min \mathcal{L}_{\text{inner}}(\theta) \end{aligned} \quad (13)$$

where  $\psi$  is the parameters of the outer LSTM,  $\theta$  is the parameters of inner-loop. Note that the outer-loop parameters  $\psi$  are shared across all sites while the inner-loop parameters  $\theta$  are specific to each site.

**Why meta-learning** Traditional methane flux prediction models either rely on globally shared parameters or fail to fully exploit historical information. In our setting, historical context must be explicitly encoded into the prediction process. However, since input drivers and labels vary dynamically across training and evaluation, efficiently integrating this information poses a challenge. Meta-learning provides a natural solution. Each site can be viewed as a distinct and evolving task, characterized by unique long-term dynamics and temporal responses. Through the inner-loop, the model learns site-specific historical information and dynamically adapts it to the outer-loop objectives, offering an effective mechanism for improving the prediction accuracy.

## 4 Evaluation

### 4.1 Experimental Setup

**Baselines.** We compare CHAM-net against nine competitive long-term time-series forecasting models. These include Transformer-based methods, such as the original Transformer [Vaswani *et al.*, 2017], iTransformer [Liu *et al.*, 2024b], Pyraformer [Liu *et al.*, 2022], DUET [Qiu *et al.*, 2025], and PatchTST [Nie *et al.*, 2022], as well as two MLP-based architectures, TSMixer [Chen *et al.*, 2023] and TimeMixer [Wang *et al.*, 2024]. We further include two RNN-based approaches, namely LSTM [Hochreiter and Schmidhuber, 1997] and P-sLSTM [Kong *et al.*, 2025]. Notably, CHAM-net can also be regarded as an RNN-based model, as it relies on BiGRU and LSTM components to extract historical information and condition the prediction.

**Datasets.** We evaluate CHAM-net and all baseline models using both simulation and observational datasets. We also consider both methane emission and consumption processes, which together constitute the natural methane cycle. Details of the datasets used in our experiments are provided below.

• **Emission Datasets.** We leverage the methane emission datasets introduced in [Sun *et al.*, 2025], which include a global simulation dataset at 0.5 degree spatial resolution with daily granularity, TEM [Zhuang *et al.*, 2004] (**TEM-E**), and an observational dataset derived from eddy covariance measurements, FLUXNET-CH4 [Delwiche *et al.*, 2021] (**FLUXNET-E**). The TEM-E dataset provides 40 years of global data spanning from 1979 to 2018. The FLUXNET-E dataset consists of measurements from 30 wetland eddy covariance tower sites, with site-specific temporal coverage determined by each site, but primarily ranging from 2006 to 2018. For each site in both TEM-E and FLUXNET-E, the datasets include 15 methane-related scalar input drivers at daily resolution, along with daily methane emission fluxes as target labels. Among these inputs, 10 are static or multi-years evolving site-specific features, including elevation (`clelev`), soil texture fractions (sand, silt, and clay) (`clfaotxt`), vegetation type (`cltveg`), soil pH value (`phh2o`), topsoil bulk density (`topsoil_bulk_density`), plant

functional type (`vegetation_type_11`), wetland type (`wetlandtype`), climate type (`climatetype`), atmospheric carbon dioxide concentration (`kco2`), and atmospheric methane concentration (`ch4`). The remaining five inputs are dynamic climate-related variables, including precipitation (`PREC`), air temperature (`TAIR`), solar radiation (`SOLR`), vapor pressure (`VAPR`), and net primary productivity (`NPP`).

• **Consumption Datasets.** We use two consumption simulation datasets, **TEM-C** [Zhuang *et al.*, 2013] and **MeMo** [Murguia-Flores *et al.*, 2018; Murguia-Flores *et al.*, 2021], which are generated by different physics-based methane consumption models that incorporate different physical processes and geographic constraints. We additionally include an observational dataset, **FLUXNET-C** [Delwiche *et al.*, 2021], which consists of methane consumption measurements from 28 upland sites collected using eddy covariance techniques. Both TEM-C and MeMo provide global coverage at 0.5 degree spatial resolution with monthly granularity data. The TEM-C dataset spans from 1979 to 2019, while MeMo covers the period from 1990 to 2009, yielding 20 years of data. The temporal coverage of FLUXNET-C varies across sites but primarily ranges from 2006 to 2018. Due to difficulties of real-world data collection, FLUXNET-C contains a limited number of missing observations (e.g., NaN consumption values in certain months for some sites). In our experiments, these missing entries are excluded from loss computation, such that predictions corresponding to NaN labels do not contribute to the optimization objective. Across all simulation and observational consumption datasets, we use a total of 18 input features. These include all drivers described in the emission datasets, along with two additional soil texture variables (`sand` and `clay`) and leaf area index (`LAI`), which characterizes vegetation cover in upland ecosystems.

**Implementation Details** All models are implemented in PyTorch 2.5.1 with CUDA 12.4. We use a learning rate of 0.001, a dropout rate of 0.2, a hidden dimension 8, three layers, 128 batch size for simulation datasets, 4 batch size for observational datasets, and the Gaussian Error Linear Unit (GELU) as the activation function [Hendrycks, 2016] among all models. For all Transformer-based models, the number of attention heads is set to 4. Other model-specific hyperparameters follow the default settings provided in the original implementations or corresponding papers. We also employ an early stopping strategy with a patience of five epochs. Each experiment is repeated three times, and the reported results are averaged across runs. All experiments are conducted using the Adam optimizer [Kingma and Ba, 2017] on a single NVIDIA GTX 3080 GPU. We provide our datasets and code in the open-source Zenodo repository<sup>1</sup>.

**Data Splitting and Evaluation Task.** We focus on temporal extrapolation for both methane emission and consumption tasks. Following [Sun *et al.*, 2025], simulation datasets are split chronologically into two equal halves, with the earlier period used for training and the later period used for test-

<sup>1</sup>Dataset and code link: <https://zenodo.org/records/20450697>.

461 ing. For example, in both the TEM-E and TEM-C datasets,  
 462 data from 1979 to 1998 are used for training, while data from  
 463 1999 to 2018 are used for testing. For the observational  
 464 datasets FLUXNET-E and FLUXNET-C, data are split on a  
 465 per-site basis, where six-sevenths of the temporal records are  
 466 used for training and the remaining one-seventh for testing.  
 467 This 6/7–1/7 split ensures sufficient training data for effective  
 468 model learning while mitigating overfitting risks.

469 **Evaluation Metrics.** We use normalized root of mean  
 470 squared error (nRMSE) and the coefficient of determination  
 471 ( $R^2$ ) to evaluate model performance. nRMSE measures the  
 472 magnitude of prediction errors normalized by the scale of the  
 473 observations, enabling fair comparison across sites with sub-  
 474 stantially different magnitudes. Lower nRMSE indicates bet-  
 475 ter performance. This metric particularly fits in our setting,  
 476 where methane fluxes vary widely across locations.  $R^2$  quan-  
 477 tifies the proportion of variance in the observations explained  
 478 by the model, reflecting its ability to capture the temporal pat-  
 479 terns. Higher  $R^2$  values correspond to a better model fit. To-  
 480 gether, nRMSE and  $R^2$  provide complementary perspectives  
 481 on predictive accuracy and pattern fidelity.

## 482 4.2 Results

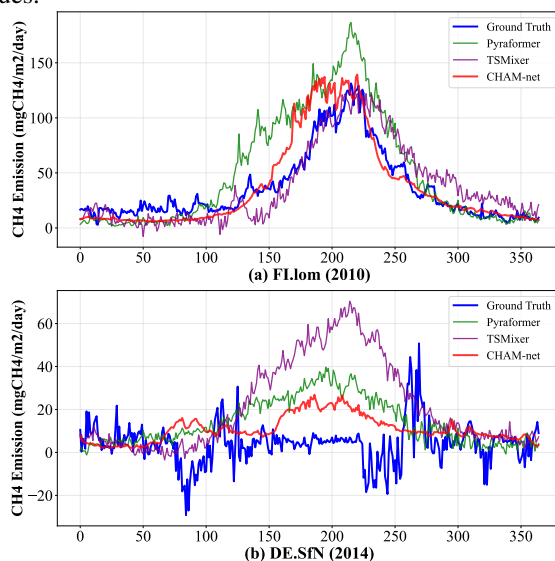
### 483 Predictive performance

484 Table 1 reports the predictive performance on all simulation  
 485 and observational datasets. For each column, models are  
 486 trained and evaluated solely on the corresponding dataset,  
 487 without pretraining or fine-tuning across datasets. We ob-  
 488 serve that CHAM-net consistently outperforms all baselines  
 489 in terms of both nRMSE and  $R^2$ . Specifically, on the emis-  
 490 sion datasets TEM-E and FLUXNET-E, CHAM-net achieves  
 491 nRMSE values of 0.43 and 0.88, respectively. The nRMSEs  
 492 are at least 0.1 lower than those of competing methods, indi-  
 493 cating its superior ability to capture the magnitude of methane  
 494 emissions over time. CHAM-net also attains the highest  $R^2$   
 495 value on FLUXNET-E, showing more accurate modeling of  
 496 the emission patterns. The combination of lower nRMSE and  
 497 higher  $R^2$  demonstrates that CHAM-net effectively captures  
 498 both emission scales and temporal dynamics, which is criti-  
 499 cal for reliable future methane budget estimation. Moreover,  
 500 the improvement reflects that the learned site-specific rep-  
 501 resentations provide valuable insights into localized emission  
 502 behavior, which can help inform targeted methane mitigation  
 503 strategies.

504 For the consumption datasets, CHAM-net demonstrates  
 505 substantial improvements on TEM-C, reducing nRMSE by  
 506 more than 0.4 and increasing  $R^2$  by over 0.2, indicating a  
 507 significant performance gain. For the MeMo dataset, which  
 508 is generated using relatively simpler biogeochemical equa-  
 509 tions and has more regular patterns, nearly all models achieve  
 510 lower nRMSE and higher  $R^2$  compared to the TEM-C dataset.  
 511 Results on both TEM-C and MeMo demonstrate that explic-  
 512 itly leveraging historical information substantially enhances  
 513 predictive performance for current-year consumption. For  
 514 the observational dataset FLUXNET-C, model performance  
 515 is generally limited due to the small magnitude of consump-  
 516 tion fluxes and high levels of environmental noise. Neverthe-  
 517 less, CHAM-net still achieves the highest  $R^2$  value of 0.31  
 518 and the lowest nRMSE of 1.27 among all methods.

### 519 Case Analysis

520 Figure 3 presents two representative site examples from the  
 521 FLUXNET-E dataset. We compare CHAM-net with the two  
 522 best baseline models, Pyraformer and TSMixer. As shown  
 523 in Figure 3 (a), CHAM-net achieves a closer match to both  
 524 the scale and temporal evolution of methane emissions at site  
 525 FI-Lom, particularly after day 200. While all three models  
 526 capture the overall temporal pattern, CHAM-net more accu-  
 527 rately estimates the peak value. In contrast, Pyraformer over-  
 528 estimates the peak value, whereas TSMixer underestimates  
 529 it. Figure 3 (b) illustrates results for site DE-SfN [Schmid  
 530 and Klatt, 2014], which represents a particularly challeng-  
 531 ing case due to the presence of negative flux values in the  
 532 ground truth. Even under this difficult setting, CHAM-net  
 533 more effectively captures the site-specific emission scale than  
 534 the baseline models, resulting in higher  $R^2$ , lower nRMSE,  
 535 and a total emission estimate that is closer to the observed  
 536 values.



537 Figure 3: Predictions on representative FLUXNET-E sites.

538 **Transfer Learning Analysis** We report the performance  
 539 results of adopting transfer learning methods (e.g., pretrain-  
 540 ing and fine-tuning). Table 2 reports the performance on  
 541 observational datasets when models are first pretrained on  
 542 the simulation datasets and then fine-tuned on observational  
 543 data. In the table, the columns correspond to the simulation  
 544 datasets used for pretraining, which are subsequently fine-  
 545 tuned on the corresponding observational emission or consump-  
 546 tion datasets. For example, TEM-E denotes pretraining  
 547 on TEM-E followed by fine-tuning on FLUXNET-E.

548 First, CHAM-net consistently outperforms all base-  
 549 line methods under the pretraining and fine-tuning set-  
 550 ting, demonstrating its strong adaptability across data do-  
 551 mains. Second, pretraining proves particularly beneficial for  
 552 methane consumption tasks. As shown in Table 2, pretrain-  
 553 ing on either TEM-C or MeMo improves both metrics. No-  
 554 tably, pretraining on TEM-C increases the  $R^2$  value from 0.31  
 555 to 0.43 in CHAM-net, indicating enhanced pattern learning  
 556 from simulation datasets. Finally, performance varies across  
 557 different pretraining sources, suggesting that the quality of  
 simulation datasets directly impacts fine-tuning effectiveness.

Table 1: Main results across all datasets and models. Each dataset is trained and evaluated from scratch. Lower nRMSE and higher  $R^2$  indicate better performance.

| Methods         | TEM-E       |             | FLUXNET-E   |             | TEM-C       |             | MeMo        |             | FLUXNET-C   |             |
|-----------------|-------------|-------------|-------------|-------------|-------------|-------------|-------------|-------------|-------------|-------------|
|                 | nRMSE       | $R^2$       | nRMSE       | $R^2$       | nRMSE       | $R^2$       | nRMSE       | $R^2$       | nRMSE       | $R^2$       |
| LSTM            | 0.57        | 0.94        | 1.08        | 0.53        | 1.56        | 0.56        | 0.22        | 0.89        | 1.31        | 0.27        |
| P-sLSTM         | 1.34        | 0.71        | 1.06        | 0.54        | 1.82        | 0.41        | 0.30        | 0.82        | 1.41        | 0.16        |
| Transformer     | 0.52        | 0.95        | 1.09        | 0.52        | 1.45        | 0.62        | 0.20        | 0.91        | 1.40        | 0.16        |
| iTransformer    | 1.24        | 0.75        | 1.29        | 0.33        | 1.64        | 0.52        | 0.29        | 0.83        | 1.36        | 0.21        |
| Pyraformer      | 0.92        | 0.87        | 1.05        | 0.56        | 1.49        | 0.60        | 0.22        | 0.89        | 1.29        | 0.29        |
| TSMixer         | 0.55        | 0.95        | 0.99        | 0.60        | 1.47        | 0.61        | 0.24        | 0.88        | 1.35        | 0.23        |
| TimeMixer       | 1.85        | 0.45        | 1.56        | 0.02        | 1.79        | 0.42        | 0.30        | 0.82        | 1.48        | 0.07        |
| PatchTST        | 1.81        | 0.48        | 1.26        | 0.36        | 1.93        | 0.33        | 0.43        | 0.62        | 1.38        | 0.20        |
| DUET            | 1.62        | 0.58        | 1.18        | 0.44        | 1.81        | 0.41        | 0.29        | 0.83        | 1.38        | 0.19        |
| <b>CHAM-net</b> | <b>0.43</b> | <b>0.97</b> | <b>0.88</b> | <b>0.68</b> | <b>0.99</b> | <b>0.82</b> | <b>0.15</b> | <b>0.95</b> | <b>1.27</b> | <b>0.31</b> |

Table 2: Performance of models pretrained on simulation datasets and fine-tuned on observational datasets.

| Methods         | TEM-E       |             | TEM-C       |             | MeMo        |             |
|-----------------|-------------|-------------|-------------|-------------|-------------|-------------|
|                 | nRMSE       | $R^2$       | nRMSE       | $R^2$       | nRMSE       | $R^2$       |
| LSTM            | 1.05        | 0.56        | 1.30        | 0.29        | 1.34        | 0.24        |
| P-sLSTM         | 1.17        | 0.45        | 1.30        | 0.28        | 1.40        | 0.17        |
| Transformer     | 1.09        | 0.52        | 1.30        | 0.29        | 1.32        | 0.27        |
| iTransformer    | 1.09        | 0.53        | 1.33        | 0.25        | 1.42        | 0.15        |
| Pyraformer      | 1.07        | 0.54        | 1.34        | 0.24        | 1.40        | 0.17        |
| TSMixer         | 1.08        | 0.53        | 1.34        | 0.24        | 1.34        | 0.24        |
| TimeMixer       | 1.39        | 0.23        | 1.41        | 0.16        | 1.45        | 0.11        |
| PatchTST        | 1.25        | 0.37        | 1.34        | 0.24        | 1.38        | 0.19        |
| DEUT            | 1.11        | 0.51        | 1.32        | 0.27        | 1.38        | 0.20        |
| <b>CHAM-net</b> | <b>0.92</b> | <b>0.66</b> | <b>1.16</b> | <b>0.43</b> | <b>1.25</b> | <b>0.34</b> |

558 Because TEM-C incorporates stronger physical constraints  
 559 and has more realistic consumption dynamics and scales, it  
 560 provides a more informative prior and leads to higher fine-  
 561 tuned performance on FLUXNET-C dataset.

### 562 Model Analysis

563 *Historical Year Length.* We first investigate the optimal  
 564 length of historical data used in the inner-loop of CHAM-  
 565 net. As shown in Figure 4, we report performance using the  
 566  $R^2$  value to compare different historical year window lengths.  
 567 We evaluate historical year lengths of 2, 4, 6, and 8 years  
 568 to determine the optimal setting for the simulation datasets  
 569 TEM-E, TEM-C, and MeMo. Due to the sparsity and vary-  
 570 ing temporal spans of the observational datasets (e.g., some  
 571 sites contain only three years of data), we use a single histor-  
 572 ical year length for FLUXNET-E and FLUXNET-C datasets  
 573 in our experiments. This setting is sufficient to yield ex-  
 574 plicit performance improvements, as demonstrated in Table  
 575 1. For the simulation datasets, Figure 4 shows that perfor-  
 576 mance varies marginally across different lengths of historical  
 577 window. Nevertheless, a four-year historical window consis-  
 578 tently achieves the best performance.

579 *Learned Representations Analysis.* To interpret the learned  
 580 representations and identify the most influential inputs, we  
 581 analyze the correlation between the learned representations  
 582 and the input variables. Using FLUXNET-E as an exam-  
 583 ple, we extract the site-specific representations for all sites  
 584 after training and apply principal component analysis (PCA)

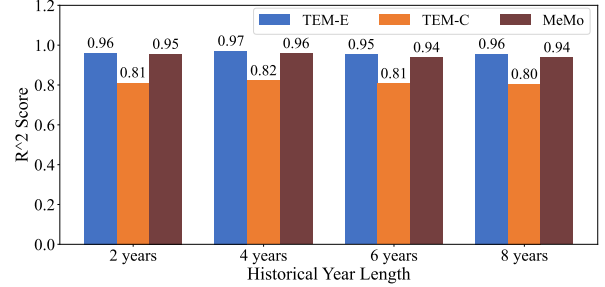


Figure 4: Sensitivity study of CHAM-net with respect to historical year length.

585 to identify the top three dominant components. We then com-  
 586 pute the Pearson product-moment correlation coefficients be-  
 587 tween these components and the site-wise input features.

588 As shown in the heatmap in Figure 5, the learned represen-  
 589 tations capture meaningful physical relationships when en-  
 590 coding historical information. In the figure, the x-axis rep-  
 591 resents the 15 input features, while the y-axis corresponds  
 592 to the three most important components identified by PCA,  
 593 namely Weight\_1 to Weight\_3. In the heatmap, positions  
 594 in read are indicative of strong associations. The results  
 595 show that topsoil bulk density, vegetation types (`cltveg`  
 596 and `vegetation_type`), climate type, solar radiation (`SOLR`),  
 597 and air temperature (`TAIR`) are among the most influential  
 598 features. These findings are consistent with the established  
 599 understanding of methane processes in natural ecosystems

600 and suggest that the learned representations can provide use-  
 601 ful insights for improved methane forecasting and mitigation  
 strategies.

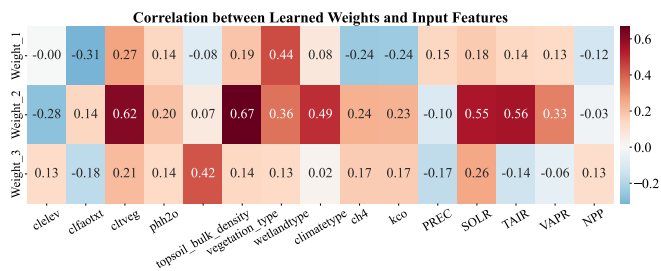


Figure 5: Correlation between learned weights and input features.

### 602 Ablation Studies

603 We also conduct the ablation experiments to examine the  
 604 contribution of each component in our framework. Using  
 605 the emission datasets as an example, we evaluate three vari-  
 606 ants of CHAM-net: (i) a mean-pooling-based CHAM-net,  
 607 (ii) CHAM-net with cross-attention, and (iii) CHAM-net with  
 608 both cross-attention and contrastive learning. For reference,  
 609 we also include the LSTM as baseline.

610 As shown in the Figure 6, the incorporation of historical  
 611 information accounts for the largest performance improve-  
 612 ment. Contrastive learning provides the second-largest gain,  
 613 as it enhances the model’s ability to distinguish site-specific  
 614 characteristics and extract informative features from histor-  
 615 ical data, leading to more expressive embeddings. Cross-  
 616 attention yields a relatively smaller improvement in this set-  
 617 ting. This is because input features evolve slowly over time,  
 618 resulting in high similarity across historical years, thus the  
 619 cross-attention offers limited benefit over mean pooling. Nev-  
 620 ertheless, cross-attention remains a configurable component  
 621 and may offer greater benefits when applied to other domains  
 622 where inputs diversity across years is more pronounced.

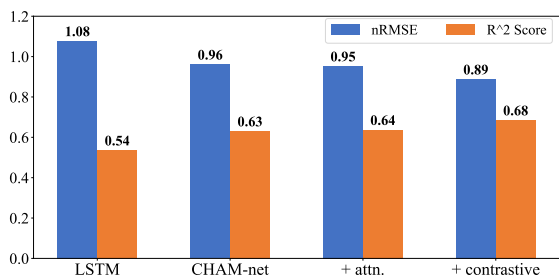


Figure 6: Ablation study of different model variants (in  $R^2$ ).

## 624 5 Related Work

625 **Methane Prediction.** Previous methane flux prediction  
 626 studies [Kim *et al.*, 2020; Irvin *et al.*, 2021; Luo *et al.*, 2023;  
 627 Chen *et al.*, 2024; Saha *et al.*, 2025] primarily rely on Ran-  
 628 dom Forest, decision tree, extreme gradient boosting (XGB),  
 629 and Artificial Neural Network (ANN) approaches trained  
 630 on relatively small observational datasets, which often fo-  
 631 cused on specific regions and coarse spatial resolutions. The

work of [Sun *et al.*, 2025] introduced the first global wet-  
 land methane emission dataset that integrates both simulation  
 and observational data, enabling large-scale machine learn-  
 ing studies. To the best of our knowledge, this work is the  
 first to jointly model methane emission and consumption in  
 natural ecosystems using machine learning, achieving state-  
 of-the-art performance and providing new insights for global  
 methane budget estimation and analysis.

**Knowledge-guided machine learning.** Knowledge-  
 guided machine learning (KGML) [Willard *et al.*, 2022;  
 Karpatne *et al.*, 2024; Yu *et al.*, 2025] has been  
 successfully applied in various environmental stud-  
 ies, including carbon dioxide modeling [Liu *et al.*,  
 2024a] and lake temperature profiling [Jia *et al.*, 2021;  
 Yu *et al.*, 2024], by embedding physical knowledge into  
 the loss functions of ML models to enhance performance.  
 While directly incorporating biogeochemical equations into  
 methane prediction models is beyond the scope of this work,  
 it represents a promising direction for future research. In  
 the supplementary material, we leverage pretraining and  
 fine-tuning to transfer knowledge from simulation datasets to  
 observational datasets, which can also be viewed as a form  
 of knowledge guidance.

## 625 6 Conclusion

In this paper, we propose a contrastive hierarchical adap-  
 tive meta-learning framework that explicitly leverages site-  
 specific historical information to capture both spatial hetero-  
 geneity and temporal dynamics in methane prediction. By  
 learning site-aware representations, our model improves pre-  
 diction accuracy for both methane emission and consumption  
 across simulation and observational datasets. These improve-  
 ments support more reliable estimation of the global methane  
 budget and provide insights that may inform effective strate-  
 gies for natural methane mitigation. Experimental results  
 demonstrate that our approach consistently outperforms all  
 other baselines, achieving the lowest nRMSE and the highest  
 $R^2$  on both methane emission and consumption datasets.

## 669 Acknowledgements

Rongchao Dong and Xiaowei Jia were partially supported  
 by the National Science Foundation (NSF) grants 2203581,  
 2239175, 2316305, 2147195, 2425845, and 2530609;  
 the USGS award G22AC00266; and the NASA grants  
 80NSSC24K1061 and 80NSSC25K0013. Licheng Liu and  
 Youmi Oh are supported by the Department of Energy  
 (DOE) grant DE-SC0024360, NSF ESII 2153040. Yiqun  
 Xie is supported in part by the NSF under Grant No.  
 2126474, 2147195, 2425844, and 2530610; NASA under  
 grant 80NSSC25K0013 and 80NSSC25K7221; Google’s AI  
 for Social Good Impact Scholars program. We also sincerely  
 thank all reviewers for their thoughtful comments and feed-  
 back, and all our collaborators for their insightful contribu-  
 tions.

684 **References**

- 685 [Bohrer and Morin, 2015] Gil Bohrer and Timothy Morin.  
686 FLUXNET-CH4 US-ORv Olentangy River Wetland Re-  
687 search Park, 2015. Dataset. Time range: 2011-2015.
- 688 [Chen *et al.*, 2023] Si-An Chen, Chun-Liang Li, Nate Yo-  
689 der, Sercan Ö. Arik, and Tomas Pfister. Tsmixer: An  
690 all-mlp architecture for time series forecasting. *CoRR*,  
691 abs/2303.06053, 2023.
- 692 [Chen *et al.*, 2024] Shuo Chen, Licheng Liu, Yuchi Ma,  
693 Qianlai Zhuang, and Narasinha J Shurpali. Quantifying  
694 global wetland methane emissions with in situ methane  
695 flux data and machine learning approaches. *Earth's Fu-*  
696 *ture*, 12(11):e2023EF004330, 2024.
- 697 [Delwiche *et al.*, 2021] Kyle B Delwiche, Sara Helen Knox,  
698 Avni Malhotra, Etienne Fluet-Chouinard, Gavin McNicol,  
699 Sarah Feron, Zutao Ouyang, Dario Papale, Carlo Trotta,  
700 Eleonora Canfora, et al. Fluxnet-ch4: A global, multi-  
701 ecosystem dataset and analysis of methane seasonality  
702 from freshwater wetlands. *Earth System Science Data Dis-*  
703 *cussions*, 2021:1–111, 2021.
- 704 [Hendrycks, 2016] D Hendrycks. Gaussian error linear units  
705 (gelus). *arXiv preprint arXiv:1606.08415*, 2016.
- 706 [Hochreiter and Schmidhuber, 1997] Sepp Hochreiter and  
707 Jürgen Schmidhuber. Long short-term memory. *Neural*  
708 *computation*, 9(8):1735–1780, 1997.
- 709 [Hospedales *et al.*, 2021] Timothy Hospedales, Antreas An-  
710 toniou, Paul Micaelli, and Amos Storkey. Meta-learning  
711 in neural networks: A survey. *IEEE transactions on pat-*  
712 *tern analysis and machine intelligence*, 44(9):5149–5169,  
713 2021.
- 714 [Irvin *et al.*, 2021] Jeremy Irvin, Sharon Zhou, Gavin McNi-  
715 col, Fred Lu, Vincent Liu, Etienne Fluet-Chouinard, Zu-  
716 tao Ouyang, Sara Helen Knox, Antje Lucas-Moffat, Carlo  
717 Trotta, et al. Gap-filling eddy covariance methane fluxes:  
718 Comparison of machine learning model predictions and  
719 uncertainties at fluxnet-ch4 wetlands. *Agricultural and*  
720 *Forest Meteorology*, 308:108528, 2021.
- 721 [Jia *et al.*, 2021] Xiaowei Jia, Jared Willard, Anuj Karpatne,  
722 Jordan S Read, Jacob A Zwart, Michael Steinbach, and  
723 Vipin Kumar. Physics-guided machine learning for scien-  
724 tific discovery: An application in simulating lake temper-  
725 ature profiles. *ACM/IMS Transactions on Data Science*,  
726 2(3):1–26, 2021.
- 727 [Karpatne *et al.*, 2024] Anuj Karpatne, Xiaowei Jia, and  
728 Vipin Kumar. Knowledge-guided machine learning:  
729 Current trends and future prospects. *arXiv preprint*  
730 *arXiv:2403.15989*, 2024.
- 731 [Kim *et al.*, 2020] Yeonuk Kim, Mark S Johnson, Sara H  
732 Knox, T Andrew Black, Higo J Dalmagro, Minseok  
733 Kang, Joon Kim, and Dennis Baldocchi. Gap-filling ap-  
734 proaches for eddy covariance methane fluxes: A com-  
735 parison of three machine learning algorithms and a tradi-  
736 tional method with principal component analysis. *Global*  
737 *Change Biology*, 26(3):1499–1518, 2020.
- [Kingma and Ba, 2017] Diederik P. Kingma and Jimmy Ba. 738  
Adam: A method for stochastic optimization, 2017. 739
- [Koebsch and Jurasinski, 2018] Franziska Koebsch and Ger- 740  
ald Jurasinski. FLUXNET-CH4 DE-Hte Huetelmoor, 741  
2018. Dataset. Time range: 2011-2018. 742
- [Kong *et al.*, 2025] Yaxuan Kong, Zepu Wang, Yuqi Nie, 743  
Tian Zhou, Stefan Zohren, Yuxuan Liang, Peng Sun, and 744  
Qingsong Wen. Unlocking the power of lstm for long 745  
term time series forecasting. In *Proceedings of the AAAI* 746  
*Conference on Artificial Intelligence*, volume 39, pages 747  
11968–11976, 2025. 748
- [Liu *et al.*, 2022] Shizhan Liu, Hang Yu, Cong Liao, Jian- 749  
guo Li, Weiyao Lin, Alex X. Liu, and Schahram Dust- 750  
dar. Pyraformer: Low-complexity pyramidal attention for 751  
long-range time series modeling and forecasting. In *The* 752  
*Tenth International Conference on Learning Representa-* 753  
*tions, ICLR 2022, Virtual Event, April 25-29, 2022*. Open- 754  
Review.net, 2022. 755
- [Liu *et al.*, 2024a] Licheng Liu, Wang Zhou, Kaiyu Guan, 756  
Bin Peng, Shaoming Xu, Jinyun Tang, Qing Zhu, Jessica 757  
Till, Xiaowei Jia, Chongya Jiang, et al. Knowledge-guided 758  
machine learning can improve carbon cycle quantification 759  
in agroecosystems. *Nature communications*, 15(1):357,  
760 2024. 761
- [Liu *et al.*, 2024b] Yong Liu, Tengge Hu, Haoran Zhang, 762  
Haixu Wu, Shiyu Wang, Lintao Ma, and Mingsheng Long. 763  
itransformer: Inverted transformers are effective for time 764  
series forecasting. In *The Twelfth International Confer-* 765  
*ence on Learning Representations, ICLR 2024, Vienna,* 766  
*Austria, May 7-11, 2024*. OpenReview.net, 2024. 767
- [Lohila *et al.*, 2010] Annalea Lohila, Mika Aurela, Juha- 768  
Pekka Tuovinen, Tuomas Laurila, Juha Hatakka, Juuso 769  
Rainne, and Timo Mäkelä. FLUXNET-CH4 FI-Lom Lom- 770  
polojankka, 2010. Dataset. Time range: 2006-2010. 771
- [Luo *et al.*, 2023] Ran Luo, Jingyi Wang, and Ian Gates. Ma- 772  
chine learning for accurate methane concentration predic- 773  
tions: short-term training, long-term results. *Environment-* 774  
*tal Research Communications*, 5(8):081003, 2023. 775
- [Malley *et al.*, 2023] Christopher S Malley, Nathan 776  
Borgford-Parnell, Seraphine Haeussling, Ioli C Howard, 777  
Elsa N Lefèvre, and Johan CI Kuylenstierna. A roadmap 778  
to achieve the global methane pledge. *Environmental* 779  
*Research: Climate*, 2(1):011003, 2023. 780
- [Mar *et al.*, 2022] Kathleen A Mar, Charlotte Unger, Lud- 781  
mila Walderdorff, and Tim Butler. Beyond co2 equiva- 782  
lence: The impacts of methane on climate, ecosystems, 783  
and health. *Environmental science & policy*, 134:127–136,  
784 2022. 785
- [Matthes *et al.*, 2018] Jaclyn Matthes, Cove Sturtevant, Patty 786  
Oikawa, Samuel Chamberlain, Daphne Szutu, Ariane Or- 787  
tiz, Joseph Verfaillie, and Dennis Baldocchi. FLUXNET- 788  
CH4 US-Myb Mayberry Wetland, 2018. Dataset. Time 789  
range: 2010-2018. 790
- [Murguia-Flores *et al.*, 2018] Fabiola Murguia-Flores, San- 791  
dra Arndt, Anita L Ganesan, Guillermo Murray-Tortarolo, 792

- 793 and Edward RC Hornibrook. Soil methanotrophy model  
794 (memo v1. 0): a process-based model to quantify global  
795 uptake of atmospheric methane by soil. *Geoscientific*  
796 *Model Development*, 11(6):2009–2032, 2018.
- 797 [Murguia-Flores *et al.*, 2021] Fabiola Murguia-Flores,  
798 Anita L Ganesan, Sandra Arndt, and Edward RC Horni-  
799 brook. Global uptake of atmospheric methane by soil  
800 from 1900 to 2100. *Global Biogeochemical Cycles*,  
801 35(7):e2020GB006774, 2021.
- 802 [Nie *et al.*, 2022] Yuqi Nie, Nam H. Nguyen, Phanwadee  
803 Sinthong, and Jayant Kalagnanam. A time series is  
804 worth 64 words: Long-term forecasting with transformers.  
805 *CoRR*, abs/2211.14730, 2022.
- 806 [Ocko *et al.*, 2021] Ilissa B Ocko, Tianyi Sun, Drew Shin-  
807 dell, Michael Oppenheimer, Alexander N Hristov,  
808 Stephen W Pacala, Denise L Mauzerall, Yangyang Xu,  
809 and Steven P Hamburg. Acting rapidly to deploy readily  
810 available methane mitigation measures by sector can im-  
811 mediately slow global warming. *Environmental Research*  
812 *Letters*, 16(5):054042, 2021.
- 813 [Qiu *et al.*, 2025] Xiangfei Qiu, Xingjian Wu, Yan Lin,  
814 Chenjuan Guo, Jilin Hu, and Bin Yang. Duet: Dual cluster-  
815 ing enhanced multivariate time series forecasting. In *Pro-*  
816 *ceedings of the 31st ACM SIGKDD Conference on Knowl-*  
817 *edge Discovery and Data Mining V. 1*, pages 1185–1196,  
818 2025.
- 819 [Saha *et al.*, 2025] Esha Saha, Oscar Wang, Amit K  
820 Chakraborty, Pablo Venegas Garcia, Russell Milne, and  
821 Hao Wang. Dispersion based recurrent neural net-  
822 work model for methane monitoring in albertan tail-  
823 ings ponds. *Journal of Environmental Management*,  
824 395:127748, 2025.
- 825 [Saunois *et al.*, 2025] Marielle Saunois, Adrien Martinez,  
826 Benjamin Poulter, Zhen Zhang, Peter A Raymond, Pierre  
827 Regnier, Josep G Canadell, Robert B Jackson, Prabir K  
828 Patra, Philippe Bousquet, et al. Global methane bud-  
829 get 2000–2020. *Earth System Science Data*, 17(5):1873–  
830 1958, 2025.
- 831 [Schmid and Klatt, 2014] Hans Schmid and Janina Klatt.  
832 FLUXNET-CH4 DE-SfN Schechenfilz Nord, 2014.  
833 Dataset. Time range: 2012-2014.
- 834 [Stocker, 2014] Thomas Stocker. *Climate change 2013: the*  
835 *physical science basis: Working Group I contribution to*  
836 *the Fifth assessment report of the Intergovernmental Panel*  
837 *on Climate Change*. Cambridge university press, 2014.
- 838 [Sun *et al.*, 2025] Yiming Sun, Shuo Chen, Shengyu Chen,  
839 Chonghao Qiu, Licheng Liu, Youmi Oh, Sparkle L Mal-  
840 one, Gavin McNicol, Qianlai Zhuang, Chris Smith, et al.  
841 X-methanewet: A cross-scale global wetland methane  
842 emission benchmark dataset for advancing science discov-  
843 ery with ai. *arXiv preprint arXiv:2505.18355*, 2025.
- 844 [Tian *et al.*, 2015] Hanqin Tian, Guangsheng Chen, Chao-  
845 qun Lu, Xiaofeng Xu, Wei Ren, Bowen Zhang, Kam-  
846 aljit Banger, Bo Tao, Shufen Pan, Mingliang Liu, et al.  
Global methane and nitrous oxide emissions from terres- 847  
trial ecosystems due to multiple environmental changes. 848  
*Ecosystem Health and Sustainability*, 1(1):1–20, 2015. 849
- [Vaswani *et al.*, 2017] Ashish Vaswani, Noam Shazeer, Niki 850  
Parmar, Jakob Uszkoreit, Llion Jones, Aidan N Gomez, 851  
Łukasz Kaiser, and Illia Polosukhin. Attention is all you 852  
need. *Advances in neural information processing systems*, 853  
30, 2017. 854
- [Wang *et al.*, 2024] Shiyu Wang, Haixu Wu, Xiaoming Shi, 855  
Tengge Hu, Huakun Luo, Lintao Ma, James Y. Zhang, and 856  
Jun Zhou. Timemixer: Decomposable multiscale mixing 857  
for time series forecasting. In *The Twelfth International*  
858 *Conference on Learning Representations, ICLR 2024, Vi-*  
859 *enna, Austria, May 7-11, 2024*. OpenReview.net, 2024. 860
- [Willard *et al.*, 2022] Jared Willard, Xiaowei Jia, Shaoming 861  
Xu, Michael Steinbach, and Vipin Kumar. Integrating sci- 862  
entific knowledge with machine learning for engineering 863  
and environmental systems. *ACM Computing Surveys*, 864  
55(4):1–37, 2022. 865
- [Yu *et al.*, 2024] Runlong Yu, Chonghao Qiu, Robert Lad- 866  
wig, Paul C Hanson, Yiqun Xie, Yanhua Li, and Xiaowei 867  
Jia. Adaptive process-guided learning: An application in 868  
predicting lake do concentrations. In *2024 IEEE Interna-*  
869 *tional Conference on Data Mining (ICDM)*, pages 580–  
870 589. IEEE, 2024. 871
- [Yu *et al.*, 2025] Runlong Yu, Chonghao Qiu, Robert Lad- 872  
wig, Paul Hanson, Yiqun Xie, and Xiaowei Jia. Physics- 873  
guided foundation model for scientific discovery: An ap- 874  
plication to aquatic science. In *Proceedings of the AAAI*  
875 *Conference on Artificial Intelligence*, volume 39, pages  
876 28548–28556, 2025. 877
- [Zhang *et al.*, 2017] Zhen Zhang, Niklaus E Zimmermann, 878  
Andrea Stenke, Xin Li, Elke L Hodson, Gaofeng Zhu, 879  
Chunlin Huang, and Benjamin Poulter. Emerging role of 880  
wetland methane emissions in driving 21st century climate 881  
change. *Proceedings of the National Academy of Sciences*, 882  
114(36):9647–9652, 2017. 883
- [Zhuang *et al.*, 2004] Qianlai Zhuang, Jerry M Melillo, 884  
David W Kicklighter, Ronald G Prinn, A David McGuire, 885  
Paul A Steudler, Benjamin S Felzer, and Shaomin Hu. 886  
Methane fluxes between terrestrial ecosystems and the at- 887  
mosphere at northern high latitudes during the past cen- 888  
tury: A retrospective analysis with a process-based bio- 889  
geochemistry model. *Global Biogeochemical Cycles*, 890  
18(3), 2004. 891
- [Zhuang *et al.*, 2013] Qianlai Zhuang, Min Chen, Kai Xu, 892  
Jinyun Tang, Eri Saikawa, Yanyu Lu, Jerry M Melillo, 893  
Ronald G Prinn, and A David McGuire. Response 894  
of global soil consumption of atmospheric methane to 895  
changes in atmospheric climate and nitrogen deposition. 896  
*Global Biogeochemical Cycles*, 27(3):650–663, 2013. 897